



Thermal performance and operational attributes of the startup characteristics of flat-shaped heat pipes using nanofluids

Karim Alizad^a, Kambiz Vafai^{a,*}, Maryam Shafahi^b

^a Department of Mechanical Engineering, University of California, Riverside, CA 92521, USA

^b Department of Mechanical Engineering, California State Polytechnic University, Pomona, CA, USA

ARTICLE INFO

Article history:

Received 5 July 2011

Received in revised form 26 August 2011

Accepted 26 August 2011

Available online 21 September 2011

Keywords:

Heat pipe

Nanofluid

Thermal performance

Flat-shaped

Disk-shaped

ABSTRACT

Thermal performance, transient behavior and operational start-up characteristics of flat-shaped heat pipes using nanofluids are analyzed in this work. Three different primary nanofluids namely, CuO, Al₂O₃, and TiO₂ were utilized in our analysis. A comprehensive analytical model, which accounts in detail the heat transfer characteristics within the pipe wall and the wick within the condensation and evaporation sections, was utilized. The results illustrate enhancement in the heat pipe performance while achieving a reduction in the thermal resistance for both flat-plate and disk-shaped heat pipes throughout the transient process. It was shown that a higher concentration of nanoparticles increases the thermal performance of either the flat-plate or disk-shaped heat pipes. We have also established that for the same heat load a smaller size flat-shaped heat pipe can be utilized when using nanofluids.

© 2011 Elsevier Ltd. All rights reserved.

1. Introduction

Heat pipes are used extensively in various applications, for achieving high rates of heat transfer utilizing evaporation and condensation processes [1–13]. Heat pipes have been used in spacecrafts, computers, solar systems, heat and ventilating air conditioning systems and many other applications [14]. The great majority of research presented in the heat pipe area addresses a cylindrical shaped geometry [1,13,15–23]. However, it has been clearly demonstrated that the flat-shaped heat pipes [2–7,9–12] have an advantage in terms of heat removal capability and geometrical adaptation for many applications such as electronic cooling, spacecraft thermal control and commercial thermal applications [2–7,10,12,24].

Most heat pipe analysis is based on the steady state operation of the device. However, in a number of applications start-up characteristics are quite important. Improper start-up can cause damage to the heat pipe. As such it is important to analyze the start-up process for the heat pipes [14]. Several transient models for the start-up of the heat pipes have been presented in the literature such as the ones by Tournier and El-Genk [22] and Chang and Colwell [25]. However, these works were all based on a regular cylindrical based geometry. The only work related to start-up process for a flat-shaped heat pipe was

presented by Zhu and Vafai [12]. They had established a comprehensive analytical solution of the startup process for asymmetrical flat-plate and disk-shaped heat pipes.

The thermophysical properties of a liquid, specifically, the thermal conductivity and heat capacity can significantly affect the heat transfer process in the liquids. Both of these properties can be augmented by dispersing the liquid with solid nanoparticles. The new liquid which now has better characteristics in transferring heat is called nanofluid [26,27]. The other properties of this liquid such as density and viscosity also change as a function of concentration of nanoparticles [1,2,28,29].

Several papers have looked at the effect of using nanofluids as a working fluid in a regular cylindrical-shaped heat pipes [1,8,15–21,23,30,31]. These works have shown enhancement in the performance of heat pipes due to a decrease in the thermal resistance when using nanofluids as a working liquid [16,17,19,20,23,31]. Thermal resistances is also affected when using different nanoparticles such as silver [15–17], CuO [8,31], nickel oxide [32], diamond [18,19], and gold [23]. The use of nanofluids results in an increase in the efficiency of the heat pipe [21] while resulting in a decline in the gradient of temperature along the heat pipe [16–18] and an improvement of the overall heat transfer coefficient [32].

Most of the research works that have investigated the use of nanofluids in heat pipes are experimental [8,15–21,23,31]. Shafahi et al. [1,2,30] utilized analytical models to investigate the thermal performance, liquid pressure, liquid velocity profile, temperature distribution of the heat pipe wall, temperature

* Corresponding author.

E-mail address: vafai@engr.ucr.edu (K. Vafai).

Nomenclature

C_p	specific heat [$\text{J kg}^{-1} \text{K}^{-1}$]	x, y, z	coordinates used in the analysis of the flat-plate heat pipe [m]
h	thickness [m]	Greek symbols	
h_{conv}	convective heat transfer coefficient [$\text{W m}^{-2} \text{K}^{-1}$]	α	thermal diffusivity [$\text{m}^2 \text{s}^{-1}$]
k	thermal conductivity [$\text{W m}^{-1} \text{K}^{-1}$]	δ	thermal layer length [m]
k_{layer}	nanolayer thermal conductivity [$\text{W m}^{-1} \text{K}^{-1}$]	ϕ	particle concentration
k_p	nanoparticles thermal conductivity [$\text{W m}^{-1} \text{K}^{-1}$]	ε	porosity of the wick
L	length of the flat-plate heat pipe [m]	η	alternative coordinate for condenser part solution
L_e	length of heat input zone of the flat-plate heat pipe [m]	θ	angular coordinate
q_l	heat flux at the wall-wick interface [W m^{-2}]	ξ	alternative coordinate for evaporator part solution
q_{in}	input heat flux at the evaporator wall outer surface [W m^{-2}]	ρ	density [kg m^{-3}]
q_e	heat flux at the evaporator liquid-vapor interface [W m^{-2}]	Subscripts	
q_c	heat flux at the condenser liquid-vapor interface [W m^{-2}]	<i>bf</i>	base fluid
r, y	the disk-shape heat pipe's radial and vertical coordinate [m]	<i>c</i>	condenser section
R	disk-shape heat pipe's radius [m]	<i>e</i>	evaporator section
R_e	disk-shape heat pipe's heat input radius [m]	<i>eff</i>	effective value for liquid-wick
t	time [s]	<i>l</i>	liquid phase
T	temperature [K]	<i>lv</i>	liquid-vapor interface
T_l	wall-wick interface temperature [K]	<i>nf</i>	nanofluid
T_i	initial temperature [K]	<i>p</i>	particle
T_∞	ambient temperature [K]	<i>v</i>	vapor section of the heat pipe
w	nanolayer thickness [nm]	<i>w</i>	wick section of the heat pipe
		<i>wa</i>	wall section of the heat pipe

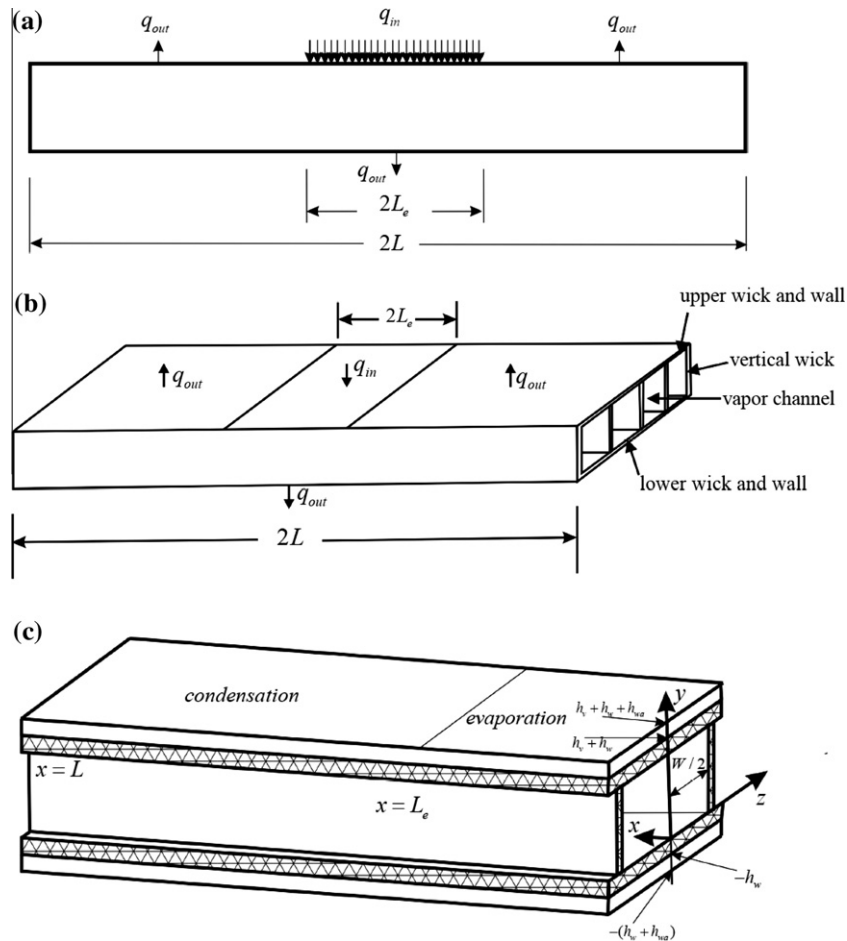


Fig. 1. Schematic of the flat-plate heat pipe: (a) side view of the heat pipe, (b) geometry of the flat-plate heat pipe, and (c) coordinate system used in the paper.

gradient along the heat pipe, thermal resistance and maximum heat load of rectangular and disk-shaped heat pipes when a nanofluid is used as the working fluid. They investigated the thermal performance of the heat pipes under steady state conditions using different concentrations of several primary nanoparticles. In the current work, a comprehensive investigation of the effect of using different nanofluids on the startup process of flat-shaped heat pipes is presented. The analysis is based on the startup model presented in Zhu and Vafai [12]. Our results show that utilizing nanofluids decreases the overall thermal resistance of the flat-shaped heat pipe. This translates into a higher thermal performance for the heat pipe. The higher thermal performance is specially more pronounced at earlier times within the startup process and decreases to a constant level as we approach the steady state conditions. These results provide for the first time, a highly effective means of investigating various attributes of the start-up process for the flat-shaped heat pipes using nanofluids.

2. Analysis and formulation

The schematics of a flat-plate and disk-shaped heat pipes used in this study are given in Figs. 1 and 2, respectively. The model utilized here is based on the comprehensive analysis performed by Zhu and Vafai [12]. The heat is conducted through the walls and saturated liquid in the wick and is eventually transferred by the vapor to the condenser section. Convection and conduction along the heat pipe are generally negligible during the transient operation of a heat pipe [33]. The prominent direction of heat transfer is along the lateral direction of the heat pipe across the wall and wick regions. The equations representing the transfer of energy within the wall and the wick regions are respectively

$$(\rho c_p)_{wa} \frac{\partial T_{wa}}{\partial t} = k_{wa} \frac{\partial^2 T_{wa}}{\partial y^2} \tag{1}$$

$$(\rho c_p)_{eff} \frac{\partial T_l}{\partial t} = k_{eff} \frac{\partial^2 T_l}{\partial y^2} \tag{2}$$

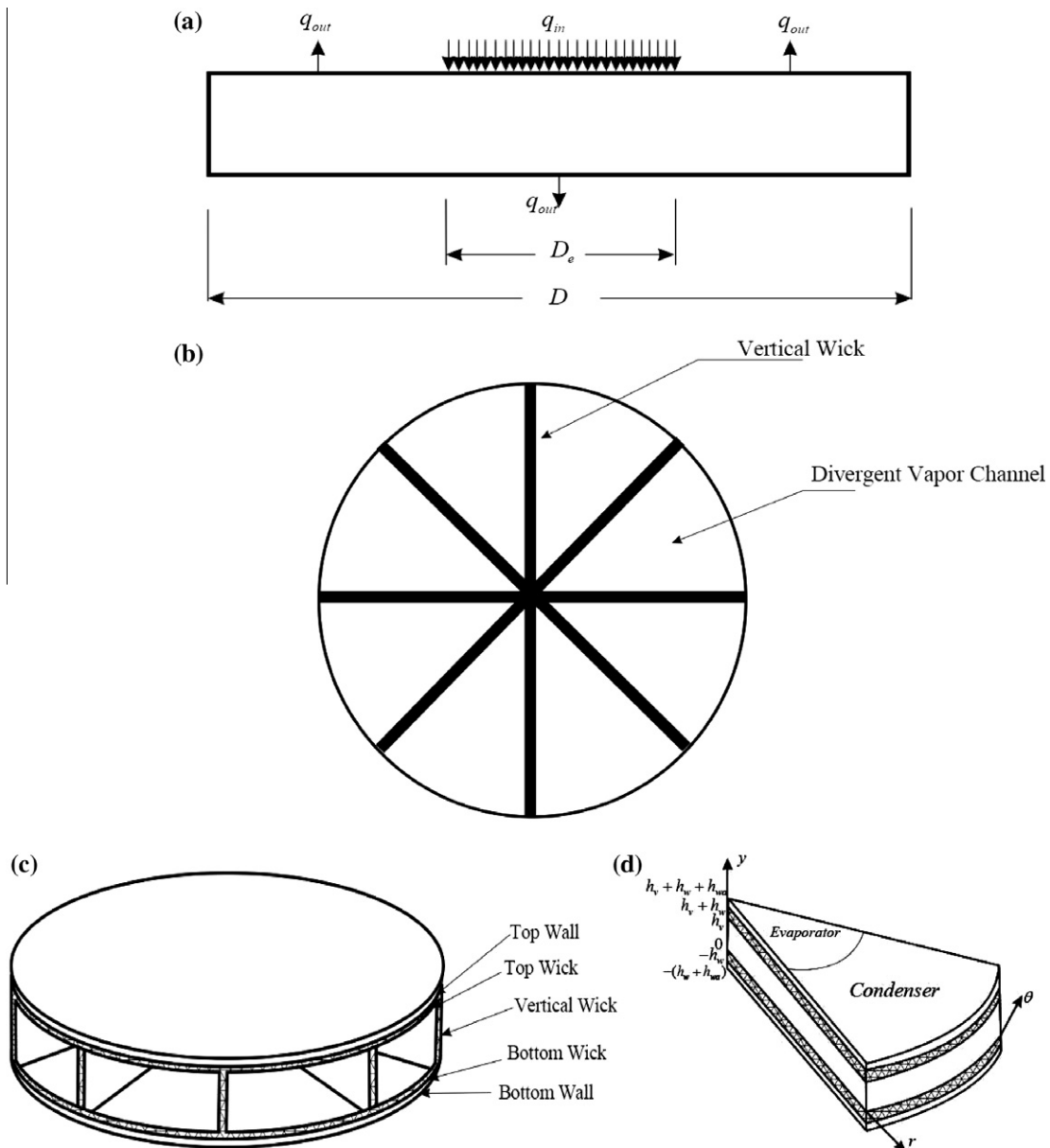


Fig. 2. Schematic of disk-shape heat pipe: (a) front view of the heat pipe, (b) top view of heat pipe, (c) geometry of disk-shape heat pipe, and (d) coordinate system of disk-shaped heat pipe used in the paper.

where the working liquid is a nanofluid and the properties related to the wick part are based on nanofluid properties modified by the porosity of the wick. These modifications for thermal conductivities are

$$k_{eff} = k_w \left[\frac{2 + k_l/k_w - 2\varepsilon_w(1 - k_l/k_w)}{2 + k_l/k_w + \varepsilon_w(1 - k_l/k_w)} \right] \quad (3)$$

$$k_{nf} = \frac{k_{pe} + 2k_{bf} + 2(k_{pe} - k_{bf})(1 + \beta)^3 \phi}{k_{pe} + 2k_{bf} - (k_{pe} - k_{bf})(1 + \beta)^3 \phi} k_{bf} \quad (4)$$

where Eq. (3) is based on the work of Dunn and Reay [34] which incorporates the porosity effect and, Eq. (4) is based on the work of Yu and Choi [35] which in turn is based on Maxwell's equation for a homogeneous suspension. In these equations liquid, and wick thermal conductivities are k_l , k_w and ε_w is the porosity of the top and bottom wicks. It should be noted that in this work, k_l is replaced with k_{nf} . The other parameters in Eq. (4) are defined as

$$k_{pe} = \frac{[2(1 - \gamma) + (1 + \beta)^3(1 + 2\gamma)]\gamma}{-(1 - \gamma) + (1 + \beta)^3(1 + 2\gamma)} k_p \quad (4a)$$

$$\gamma = \frac{k_{layer}}{k_p}; \quad \beta = \frac{w}{r_p} \quad (4b)$$

where k_{layer} and k_p are thermal conductivities of the nanolayer and nanoparticles. This equation is based on the assumptions that the

nanolayer around the particles is more conductive than the liquid and the nanolayers around these particles don't overlap due to their low volume concentration [35].

The heat capacity of nanofluids can be obtained based on the mixing theory for ideal gas mixtures as [36]

$$(\rho C_p)_{nf} = (1 - \phi)(\rho C_p)_{bf} + \phi(\rho C_p)_p \quad (5)$$

and [12],

$$(\rho C_p)_{eff} = \varepsilon_w(\rho C_p)_w + (1 - \varepsilon_w)(\rho C_p)_l \quad (6)$$

where $(\rho C_p)_w$ is the heat capacity for bottom and top wicks within the heat pipe. It should be noted that in this work, $(\rho C_p)_l$ is replaced with $(\rho C_p)_{nf}$.

The boundary condition at the evaporator part and outer wall surface (at $y = h_v + h_w + h_{wa}$ and $0 \leq r \leq R_e$ for the disk shaped and $0 \leq x \leq L_e$ for the flat-plate heat pipe) is given as:

$$k_{wa} \frac{\partial T_{wa}}{\partial y} \Big|_{y=h_v+h_w+h_{wa}} = q_{in} \quad (7)$$

Boundary conditions for the condenser part are applied over two sections. First for the upper part of the condenser which is at $y = h_v + h_w + h_{wa}$ and $R_e \leq r \leq R$ for the disk-shaped and $L_e \leq x \leq L$ for the flat-plate heat pipe,

$$-k_{wa} \frac{\partial T_{wa}}{\partial y} \Big|_{y=h_v+h_w+h_{wa}} = h_{conv}(T_{wa}(y = h_v + h_w + h_{wa}, t) - T_\infty) \quad (8)$$

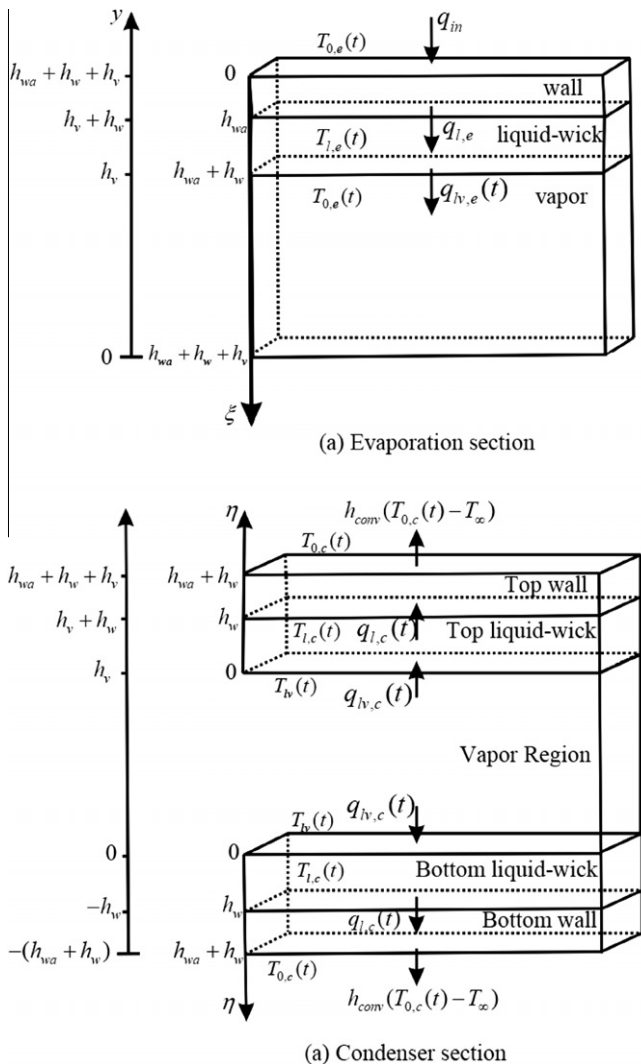


Fig. 3. Alternative coordinate systems used in the paper.

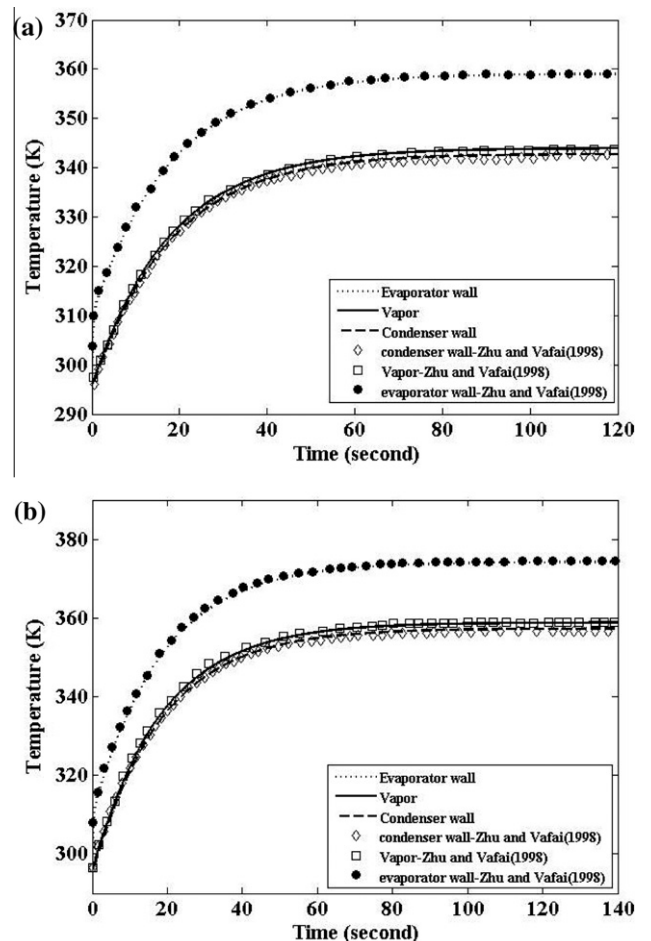


Fig. 4. Comparison of the results for flat-plate and disk-shaped heat pipes with the existing results presented by Zhu and Vafai [12]

and for the lower part of the condenser which is at $y = -(h_w + h_{wa})$ and $0 \leq r \leq R$ for the disk-shaped and $0 \leq x \leq L$ for the flat-plate heat pipe,

$$-k_{wa} \frac{\partial T_{wa}}{\partial y} \Big|_{y=-(h_w+h_{wa})} = h_{conv}(T_{wa}(y=-(h_w+h_{wa}), t) - T_\infty) \quad (9)$$

where T_∞ is the temperature of the coolant and h_{conv} is the convective heat transfer coefficient of the coolant.

The boundary conditions at the wall-wick interfaces for both top and bottom wicks which are located at $y = (h_w + h_v)$ and $y = -h_w$ can be presented as

$$\begin{aligned} T_{wa}(y = h_v + h_w, t) &= T_l(y = h_v + h_w, t) \\ T_{wa}(y = -h_w, t) &= T_l(y = -h_w, t) \end{aligned} \quad (10)$$

$$\begin{aligned} k_{wa} \frac{\partial T_{wa}}{\partial y} \Big|_{y=h_v+h_w} &= k_w \frac{\partial T_l}{\partial y} \Big|_{y=h_v+h_w} \\ k_{wa} \frac{\partial T_{wa}}{\partial y} \Big|_{y=-h_w} &= k_w \frac{\partial T_l}{\partial y} \Big|_{y=-h_w} \end{aligned} \quad (11)$$

The temperature and heat flux jump boundary conditions at liquid-vapor interfaces are applied at $y = 0$ and $y = h_v$ resulting in

$$\begin{aligned} T_v(y = 0, t) &= T_l(y = 0, t) \\ T_v(y = h_v, t) &= T_l(y = h_v, t) \end{aligned} \quad (12)$$

$$\begin{aligned} k_w \frac{\partial T_l}{\partial y} \Big|_{y=h_v} &= k_v \frac{\partial T_v}{\partial y} \Big|_{y=h_v} \\ k_w \frac{\partial T_l}{\partial y} \Big|_{y=0} &= k_v \frac{\partial T_v}{\partial y} \Big|_{y=0} \end{aligned} \quad (13)$$

Since both heat flux and temperature at liquid-vapor are not specified, guessed values can initially be used. A marching scheme in time is implemented utilizing an initial condition specified by

$$T_{wa} = T_l = T_v = T_i \quad \text{at } t = 0. \quad (14)$$

Analytical solution for the unsteady energy equation covers four regimes/parts in order to capture the physics of the start-up operation of the heat pipe. The first part is for the initial advancement of the thermal front from the heat source in the evaporator section into the wall, the second part covers the solution for the temperature distribution within the wick region when the thermal front reaches the liquid-solid interface between the wall and wick regions. The third part of the solution captures the physics of the process when the thermal front reaches the liquid-vapor interface and the transport within the wick part of the condenser and the fourth part of solution describes the thermal front which reaches the wall section of condenser while incorporating the convective cooling with the outside fluid.

The solution for the wall and wick regions starts with integration of Eqs. (1) and (2) with respect to y from the heat pipe wall to distance $\delta_c(t)$ for the evaporator section while temperature remains unaffected for the other regions. After this thermal layer crosses the wick region and reaches the liquid-vapor interface, the integration domain will be based on the entire wall and wick regions. Using the interface boundary conditions (12) and (13) along with the properly integrated governing equations will result in the temperature distribution within these regions.

A new coordinate system is adopted to simplify the integration process. This coordinate system is defined as $\xi = h_v + h_w + h_{wa} - y$ and is shown in Fig. 3(a). Using this coordinate system, governing equations (1) and (2) can be recast as:

$$(\rho c_p)_{wa} \frac{\partial T_{wa}}{\partial t} = k_{wa} \frac{\partial^2 T_{wa}}{\partial \xi^2} \quad \text{for } 0 \leq \xi \leq h_{wa}, t \geq 0 \quad (15)$$

$$(\rho c_p)_{eff} \frac{\partial T_l}{\partial t} = k_{eff} \frac{\partial^2 T_l}{\partial \xi^2} \quad \text{for } h_{wa} \leq \xi \leq h_{wa} + h_w, t \geq 0 \quad (16)$$

A second order polynomial approximation is used to represent the temperature distribution as:

$$T(\xi, t) = a_0(t) + a_1(t)\xi + a_2(t)\xi^2 \quad (17)$$

The solution for evaporator section of the wall consists of three parts. The first part starts from the moment, $t = 0$, the evaporator

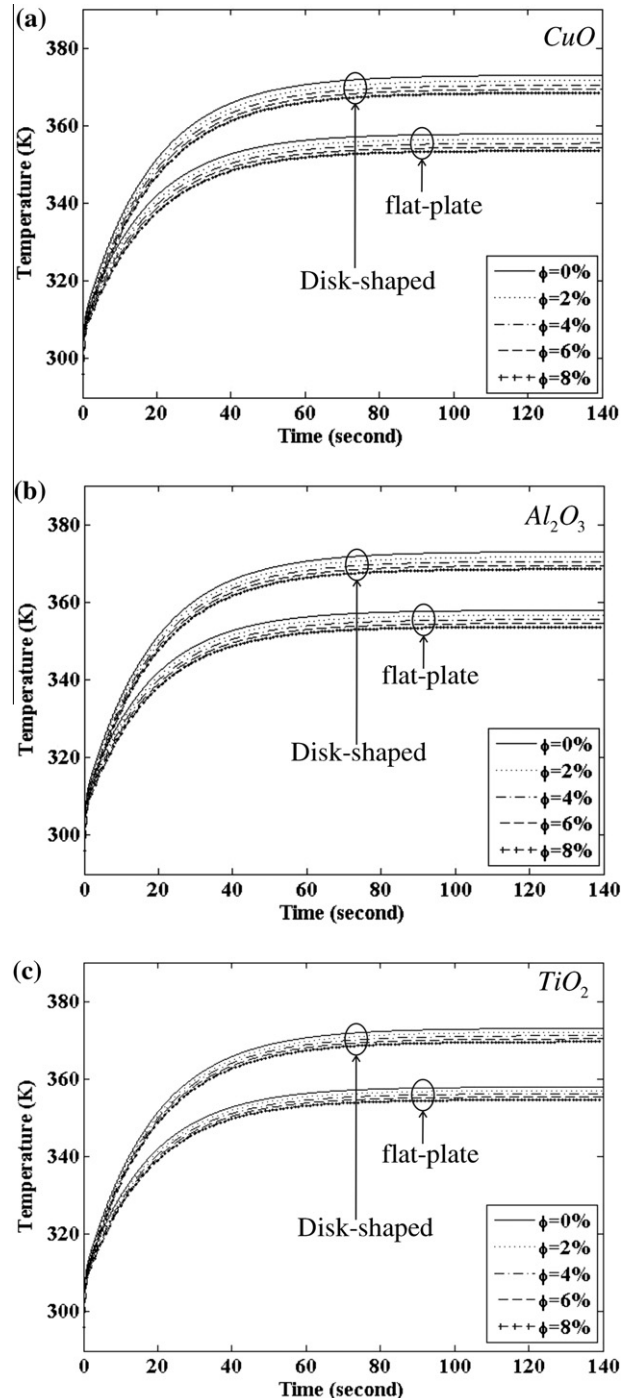


Fig. 5. Transient response of flat-shaped heat pipe wall temperature for different level of concentrations for nanoparticles (a) CuO, (b) Al₂O₃, and (c) TiO₂.

external wall experiences the imposed heat load, and continues on while the thermal front penetrates through the wall. During this part the wick and vapor regions remain unaffected by the advancing thermal front within the external wall. For this time period when the thermal layer has not reached the wall–wick interface $\delta_e(t) \leq h_{wa}$, the boundary conditions are

$$\begin{aligned}
 -k_{wa} \frac{\partial T_{wa}}{\partial \xi} \Big|_{\xi=0} &= q_{in} \\
 T_{wa}(\xi = \delta_e(t), t) &= T_i \\
 \frac{\partial T_{wa}}{\partial \xi} \Big|_{\xi=\delta_e(t)} &= 0
 \end{aligned}
 \tag{18}$$

Imposing the boundary conditions given by Eq. (18) on the temperature profile given by Eq. (17) results in

$$T_{wa}(\xi, t) = T_i + \frac{q_{in} \delta_e(t)}{2k_{wa}} \left(1 - \frac{\xi}{\delta_e(t)}\right)^2 \quad 0 \leq \xi \leq \delta_e(t)
 \tag{19}$$

The temporal growth of the thermal layer for this part can be determined by using Eq. (19) in the integrated form of Eq. (15) and using the initial condition, resulting in:

$$\delta_e(t) = \sqrt{6\alpha_{wa}t}
 \tag{20}$$

As can be seen the growth of the thermal layer for this part is dependent on time and thermal diffusivity of the wall $\alpha_{wa} = k_{wa}/(\rho c_p)_{wa}$. This can be combined with Eq. (19) to get the temperature distribution within the wall of the evaporator. The time that it takes for this thermal layer to reach the wall–wick interface is

$$t_1 = \frac{h_{wa}^2}{6\alpha_{wa}}
 \tag{21}$$

The second part of solution is for the time period when the thermal layer reaches the wall–wick interface and starts penetrating within the wick region while the temperature inside the evaporator wall is still increasing with time. In this part, the vapor temperature remains constant. The boundary conditions for the thermal layer growing in the liquid saturated wick region, $h_{wa} < \delta_e^*(t) \leq h_{wa} + h_w$, can be specified as

$$\begin{aligned}
 T_l(\xi = h_{wa}, t) &= T_{l,e}(t) \\
 T_l(\xi = \delta_e^*(t), t) &= T_i \\
 \frac{\partial T_l}{\partial \xi} \Big|_{\xi=\delta_e^*(t)} &= 0
 \end{aligned}
 \tag{22}$$

and the boundary conditions for the wall part during this time period are:

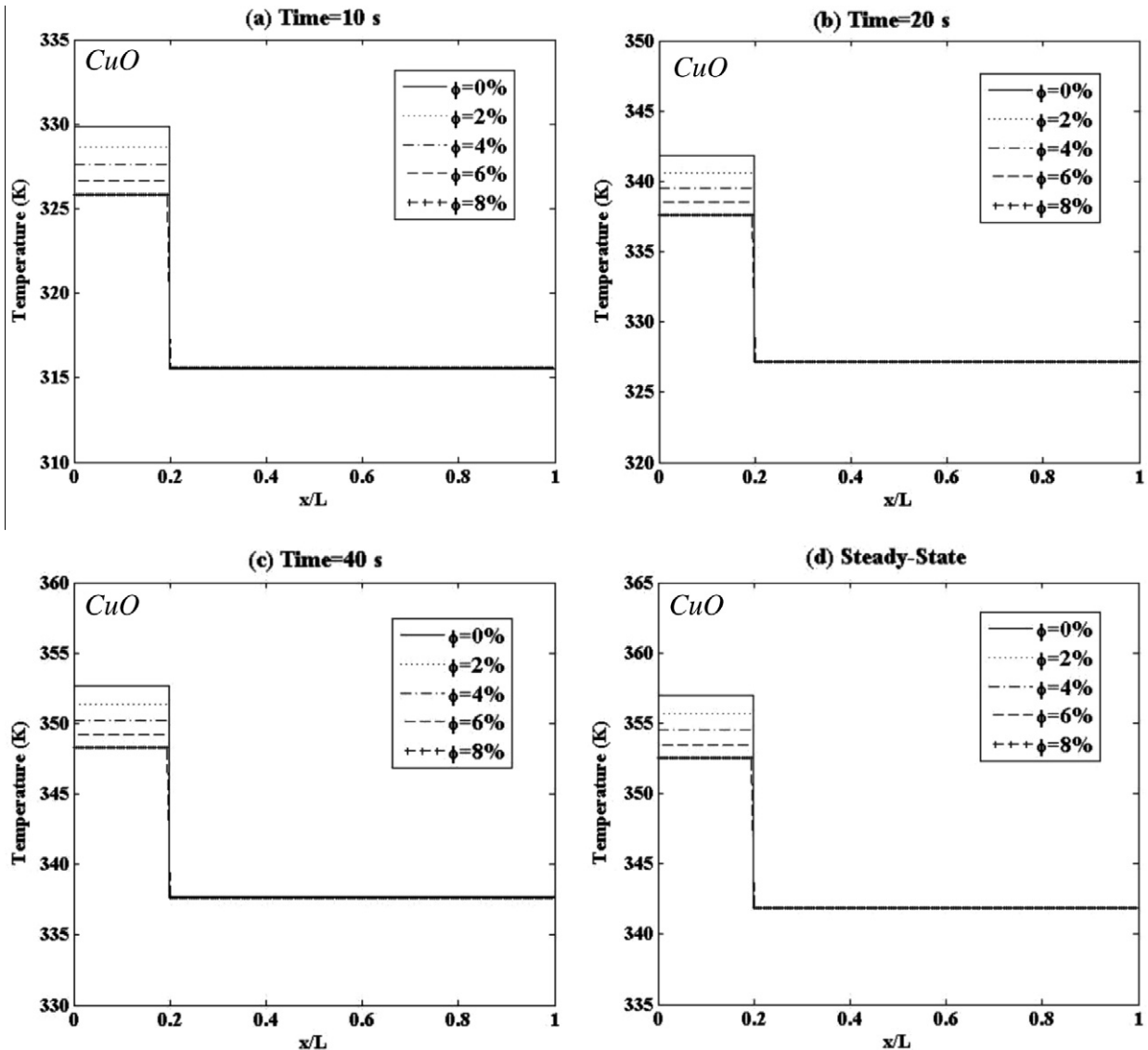


Fig. 6. Flat-plate heat pipe temperature profile for different concentrations of CuO in: (a) 10 s (b) 20 s (c) 40 s and (d) steady state condition.

$$\begin{aligned}
 -k_{wa} \frac{\partial T_{wa}}{\partial \xi} \Big|_{\xi=0} &= q_{in} \\
 T_{wa}(\xi = h_{wa}, t) &= T_{l,e}(t) \\
 -k_{wa} \frac{\partial T_{wa}}{\partial \xi} \Big|_{\xi=h_{wa}} &= q_{l,e}(t)
 \end{aligned}
 \tag{23}$$

where $q_{l,e}(t)$ and $T_{l,e}(t)$ are the heat flux and the temperature at the wall–wick interface of the evaporator region and $\delta_e^*(t)$ is the thermal layer within the wick part of the evaporator.

Using the temperature profile given by Eq. (17) and substituting the wall boundary conditions given by Eq. (23), the final temperature distribution for wall in this period of time is obtained as

$$\begin{aligned}
 T_{wa}(\xi, t) &= T_{l,e}(t) + \frac{q_{in}}{2\lambda_{wa}} \left(1 - \frac{\xi}{h_{wa}}\right)^2 + \frac{q_{l,e}(t)}{2\lambda_{wa}} \left[1 - \left(\frac{\xi}{h_{wa}}\right)^2\right] \\
 0 \leq \xi \leq h_{wa}, \quad t_1 \leq t \leq t_2
 \end{aligned}
 \tag{24}$$

where $\lambda_{wa} = k_{wa}/h_{wa}$ and t_2 is the time period for thermal layer to reach the liquid–vapor interface. The temperature distribution for saturated liquid in the wick region depends on the growing thermal layer in the wick part. Using the same temperature profile given by Eq. (17) and the boundary conditions given by Eq. (22) yields

$$\frac{T_l(\xi, t) - T_i}{T_{l,e}(t) - T_i} = \left(1 - \frac{\xi - h_{wa}}{\delta_e^*(t) - h_{wa}}\right)^2, \quad h_{wa} \leq \xi \leq \delta_e^*(t), \quad t_1 \leq t \leq t_2
 \tag{25}$$

Applying Eq. (11) which is the continuity of heat flux at the wall–wick interface results in

$$T_{l,e}(t) = T_i + \frac{q_{l,e}}{2k_{eff}} (\delta_e^*(t) - h_{wa})
 \tag{26}$$

Integrating the energy equations (15) and (16) using the temperature profiles (24) and (25) will yield two unknowns $\delta_e^*(t)$ and $q_{l,e}$. Using Eq. (25) in the energy equation (16) and integrating it with respect to ξ from h_{wa} to $\delta_e^*(t)$ while implementing boundary conditions (22) leads to the following first order differential equation:

$$(\delta_e^*(t) - h_{wa}) \frac{dT_{l,e}(t)}{dt} + (T_{l,e} - T_i) \frac{d\delta_e^*(t)}{dt} = \frac{6\alpha_{eff}(T_{l,e}(t) - T_i)}{\delta_e^*(t) - h_{wa}}
 \tag{27}$$

where $\alpha_{eff} = k_{eff}/(\rho c_p)_{eff}$ is the saturated liquid effective diffusivity. Deriving an expression for $\frac{dT_{l,e}(t)}{dt}$ and solving the differential equation while implementing the initial condition as $\delta_e^*(t_1) = h_{wa}$ where $t_1 = \frac{h_{wa}^2}{6\alpha_{wa}}$ as given in (21) yields the first unknown as

$$\delta_e^*(t) = h_{wa} + \sqrt{8\alpha_{eff}(t - t_1)}
 \tag{28}$$

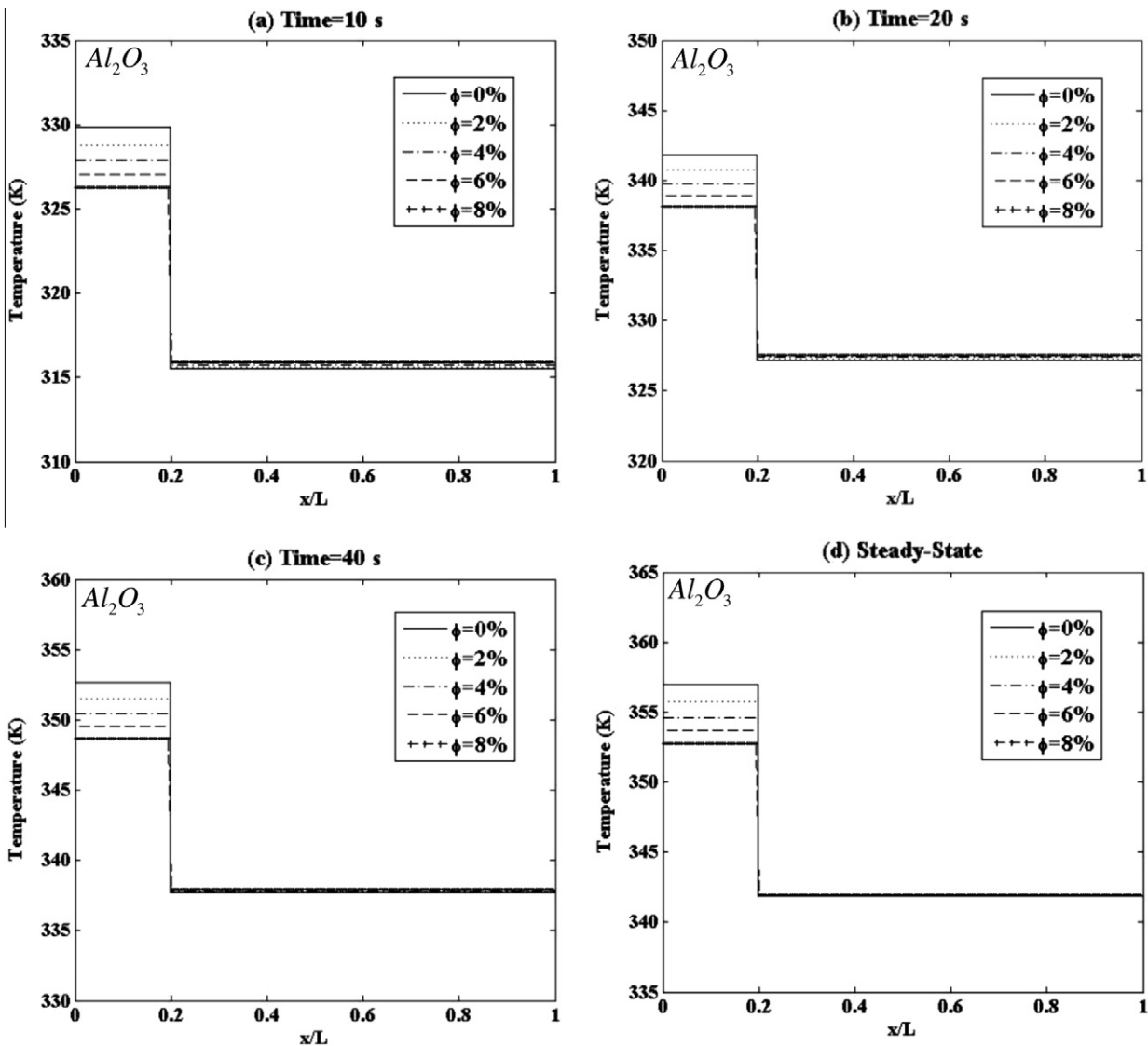


Fig. 7. Flat-plate heat pipe temperature profile for different concentrations of Al_2O_3 in: (a) 10 s (b) 20 s (c) 40 s and (d) steady state condition.

Hence the time for this thermal layer to reach the liquid–vapor interface is

$$t_2 = t_1 + \frac{h_w^2}{8\alpha_{eff}} \quad (29)$$

Using Eqs. (26) and (27) and the temperature profile given by Eq. (24) and substituting these in the integrated form of the energy Eq. (16) with respect to ξ from 0 to h_{wa} while applying the boundary conditions given by Eq. (23) and initial conditions, $\delta_e^*(t_1) = h_{wa}$ and $q_{l,e}(t_1) = 0$, results in

$$q_{l,e}(t) = \frac{q_{in}}{A(t)} (t - t_1) \quad (30)$$

where

$$A(t) = \frac{(\delta_e^*(t) - h_{wa})^2}{6\alpha_{eff}} + \frac{k_{wa}h_{wa}}{2k_{eff}\alpha_{wa}} (\delta_e^*(t) - h_{wa}) + \frac{h_{wa}^2}{3\alpha_{wa}} \quad (31)$$

The third part of the solution starts when the thermal layer inside the wick reaches the liquid–vapor region. This occurs for $t > t_2$ when the evaporation starts at the liquid–vapor interface while the temperature within the wall and the liquid inside wick keep on

increasing. Due to the low temperature gradient within the vapor phase for low-temperature heat pipes [4,33], the vapor temperature can be considered to be the same as liquid–vapor interface temperature during this time period. As such the load imposed at the evaporator section is transported unaltered via the vapor to the condenser section. Furthermore, due to the short transient time between evaporator and condenser sections, a quasi-steady model is used for the vapor part. The above-cited physical attributes enable the determination of the vapor temperature.

For $t > t_2$ the boundary conditions for the saturated liquid within the wick as the heat is transferred from the wall to the liquid and the liquid thermal layer reaches the liquid–vapor interface can be expressed as

$$\begin{aligned} T_l(\xi = h_{wa}, t) &= T_{l,e}(t) \\ -k_{eff} \frac{\partial T_l}{\partial \xi} \Big|_{\xi=h_{wa}} &= q_{l,e}(t) \\ T_l(\xi = h_{wa} + h_w, t) &= T_{lv}(t) \end{aligned} \quad (32)$$

where T_{lv} is the temperature at the liquid–vapor interface which is the same as vapor temperature. The boundary conditions for the wall section are the same as that given in Eq. (23) since there is

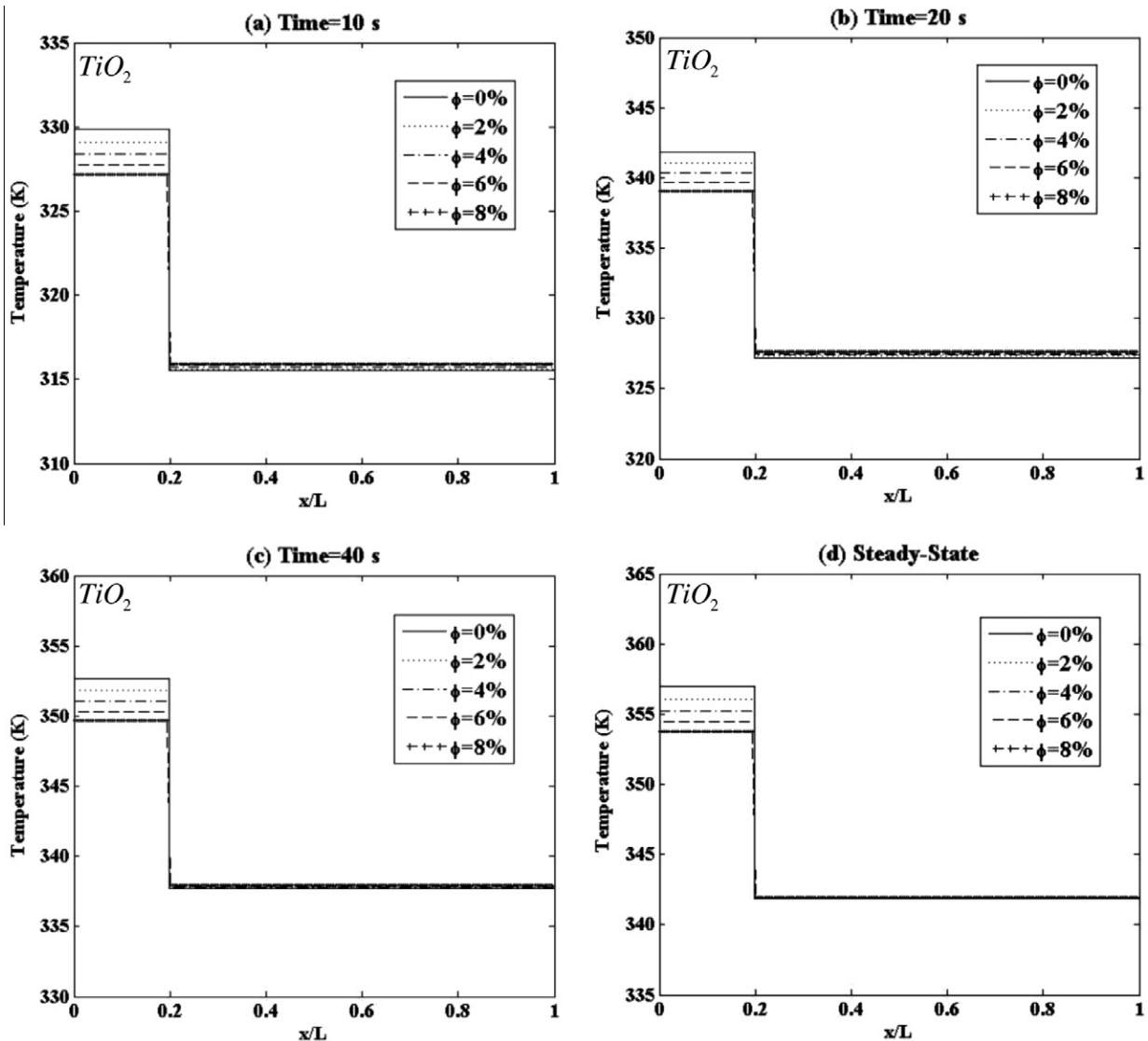


Fig. 8. Flat-plate heat pipe temperature profile for different concentrations of TiO_2 in: (a) 10 s (b) 20 s (c) 40 s and (d) steady state condition.

no change for this part. Using the temperature profile (17) and implementing boundary conditions given by Eqs. (23) and (32) yields the temperature distribution in the wall as follows

$$T_{wa}(\xi, t) = T_{l,e}(t) + \frac{q_{in}}{2\lambda_{wa}} \left(1 - \frac{\xi}{h_{wa}}\right)^2 + \frac{q_{l,e}(t)}{2\lambda_{wa}} \left[1 - \left(\frac{\xi}{h_{wa}}\right)^2\right], \quad 0 \leq \xi \leq h_{wa}, \quad t > t_2 \quad (33)$$

This temperature profile is the same as Eq. (24) but it relates to a different time and different values of the time-related variables. For the wick part using the second order polynomial temperature distribution and boundary conditions given by Eq. (32) results in

$$T_l(\xi, t) = T_{lv}(t) - (T_{lv}(t) - T_{l,e}(t)) \left[1 - \left(\frac{\xi - h_{wa}}{h_w}\right)^2\right] - \frac{q_{l,e}(t)}{\lambda_{eff}} \frac{\xi - h_{wa}}{h_w} \left(1 - \frac{\xi - h_{wa}}{h_w}\right) \quad h_{wa} \leq \xi \leq h_{wa} + h_w, \quad t > t_2 \quad (34)$$

where $\lambda_{eff} = k_{eff}/h_w$.

Utilizing the temperature profiles given by Eqs. (33) and (34) within the integral form of the energy equations (15) and (16) over the wall and wick sections can result in two differential equations

for the two unknowns $q_{l,e}(t)$ and $T_{l,e}(t)$. These two first order differential equations are

$$\frac{dq_{l,e}(t)}{dt} = \left\{ \frac{dT_{lv}(t)}{dt} - \left(\frac{2\alpha_{wa}}{k_{wa}h_{wa}} + \frac{6\alpha_{eff}}{k_{eff}h_w} \right) q_{l,e}(t) + \frac{6\alpha_{eff}}{h_w^2} (T_{l,e}(t) - T_{lv}(t)) + \frac{2\alpha_{wa}}{k_{wa}h_{wa}} q_{in} \right\} / \left(\frac{2}{3\lambda_{wa}} + \frac{1}{2\lambda_w} \right) \quad (35)$$

and

$$\frac{dT_{l,e}(t)}{dt} = \frac{1}{3\lambda_{wa} + 4\lambda_{eff}} \left\{ 3 \left(\frac{4\alpha_{eff}}{h_w^2} - \frac{\alpha_{wa}}{h_{wa}^2} \right) q_{l,e}(t) + \frac{3\alpha_{wa}}{h_{wa}^2} q_{in} - 2\lambda_{eff} \left[\frac{dT_{lv}(t)}{dt} + \frac{6\alpha_{eff}}{h_w^2} (T_{l,e}(t) - T_{lv}(t)) \right] \right\} \quad (36)$$

Based on the energy equation at liquid–vapor interface it can be shown that the heat flux at that interface can be written as:

$$q_{lv,e}(t) = \frac{2k_{eff}}{h_w} [T_{l,e}(t) - T_{lv}(t)] - q_{l,e}(t) \quad (37)$$

In the condenser section of the heat pipe, energy transfer starts after $t = t_2$ when the vapor condenses as a result of temperature

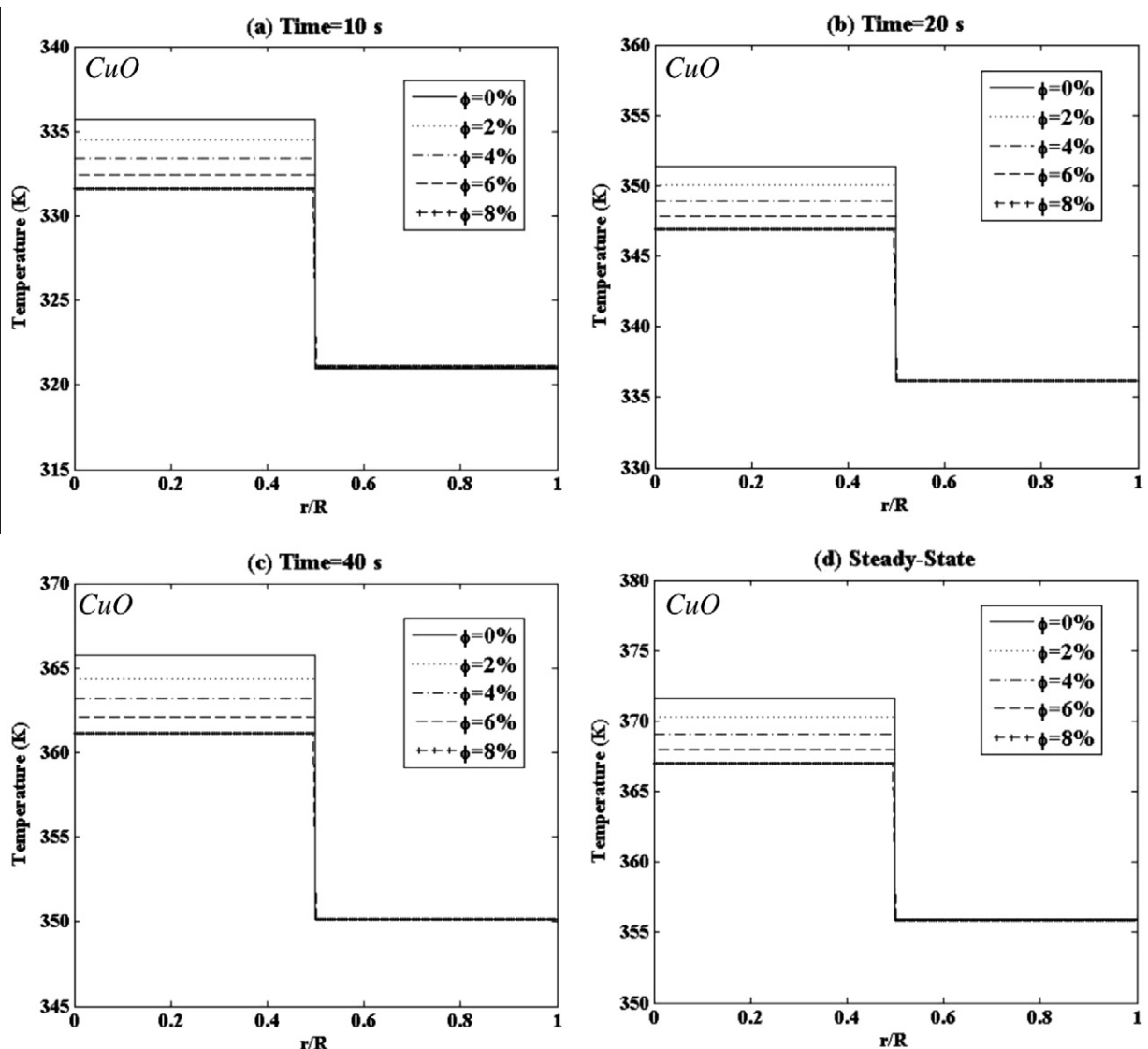


Fig. 9. Disk-shape heat pipe temperature profile for different concentrations of CuO in: (a) 10 s (b) 20 s (c) 40 s and (d) steady state condition.

gradient between vapor and the liquid within the wick region at the condenser section. This transfer of energy initiates a thermal layer within the liquid that proceeds towards the wick–solid interface. Since the direction of growth in the condenser section is opposite of that in the evaporator section, a new coordinate system is introduced to better capture the physics of the process. As such for the top wall and the condenser’s wick, we introduce $\eta = y - h_w$ and for the bottom condenser’s wall and the wick, $\eta = -y$ is introduced as shown in Fig. 3(b). The modified energy equations can be written as follows

$$(\rho C_p)_{wa} \frac{\partial T_{wa}}{\partial t} = k_{wa} \frac{\partial^2 T_{wa}}{\partial \eta^2}, \quad \text{for } h_w \leq \eta \leq h_w + h_{wa}, \quad t > t_2 \quad (38)$$

$$(\rho C_p)_{eff} \frac{\partial T_l}{\partial t} = k_{eff} \frac{\partial^2 T_l}{\partial \eta^2}, \quad \text{for } 0 \leq \eta \leq h_w, \quad t > t_2 \quad (39)$$

For the wall and wick parts of condenser, the solution can be separated into three regimes: (1) growth of the thermal layer within the wick before reaching the wall–wick interface, (2) this part deals with the energy after the thermal layer reaches the wall–wick interface while the temperature keeps on increasing

within the wick region. The thermal layer keeps on advancing through the wall, (3) finally for the last part; the outer wall initiates communication with the outside fluid when thermal layer reaches this point. The second order polynomial for the temperature distribution based on the new variable η can be written as

$$T(\eta, t) = a_0(t) + a_1(t)\eta + a_2(t)\eta^2 \quad (40)$$

During the first stage the thermal layer progresses through the wick $\delta_c(t) < h_w$ and the applicable boundary conditions are

$$\begin{aligned} T_l(\eta = 0, t) &= T_{lv}(t) \\ T_l(\eta = \delta_c(t), t) &= T_i \\ \left. \frac{\partial T_l}{\partial \eta} \right|_{\eta = \delta_c(t)} &= 0 \end{aligned} \quad (41)$$

Applying the boundary conditions (41) in Eq. (40) results in

$$\frac{T_l(\eta, t) - T_i}{T_{lv}(\eta, t) - T_i} = \left(1 - \frac{\eta}{\delta_c(t)}\right)^2, \quad 0 \leq \eta \leq \delta_c(t), \quad t > t_2 \quad (42)$$

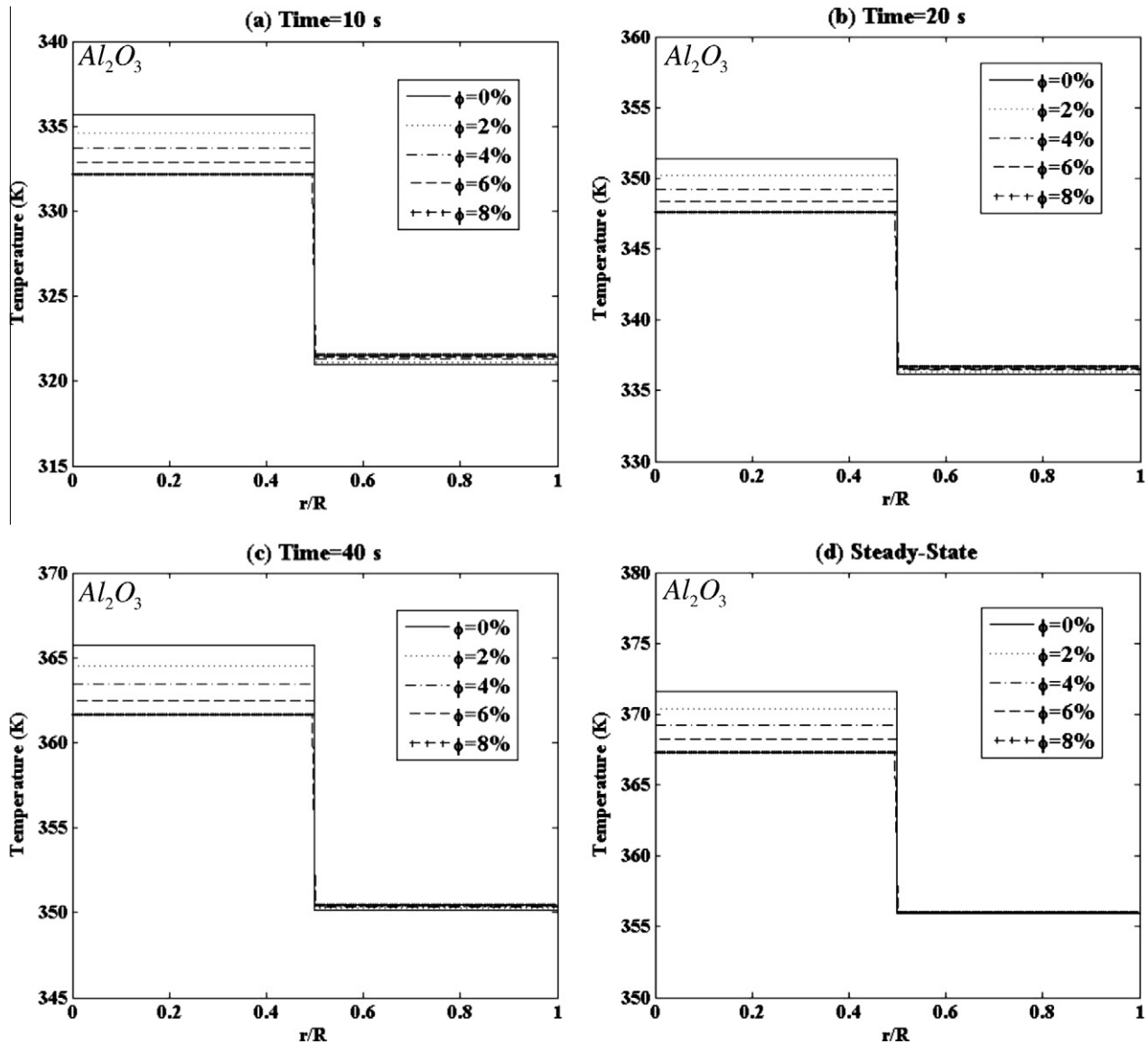


Fig. 10. Disk-shape heat pipe temperature profile for different concentrations of Al_2O_3 in: (a) 10 s (b) 20 s (c) 40 s and (d) steady state condition.

The unknown $\delta_c(t)$ can be solved, by integrating the energy Eq. (39) from 0 to $\delta_c(t)$ with respect to η and using the initial condition $\delta_c(t = t_2) = 0$:

$$\delta_c(t) = \sqrt{8\alpha_{eff}(t - t_2)} \tag{43}$$

The time that it takes for the thermal layer to reach the wall-wick interface is obtained using Eq. (43):

$$t_3 = t_2 + \frac{h_w^2}{8\alpha_{eff}} \tag{44}$$

For heat flux at the vapor–liquid interface, the energy equation in that region for this time period results in

$$q_{lw,c}(t) = \frac{2k_{eff}(T_{lv}(t) - T_i)}{\sqrt{8\alpha_{eff}(t - t_2)}} \tag{45}$$

The second stage of the solution within the condenser section captures the growth of the thermal layer within the wall section. During this stage, the temperature within the wick region keeps

on increasing. The thermal layer starts to expand after $t = t_3$ within the region specified by $h_w \leq \delta_c^*(t) \leq h_w + h_{wa}$. The boundary conditions for the liquid part can be presented as

$$\begin{aligned} T_l(\eta = 0, t) &= T_{lv}(t) \\ T_l(\eta = h_w, t) &= T_{l,c}(t) \\ -k_{eff} \frac{\partial T_l}{\partial \eta} \Big|_{\eta=h_w} &= q_{l,c}(t) \end{aligned} \tag{46}$$

and for the wall section, the boundary conditions can be presented as:

$$\begin{aligned} T_{wa}(\eta = h_w, t) &= T_{l,c}(t) \\ T_{wa}(\eta = \delta_c^*(t), t) &= T_i \\ \frac{\partial T_{wa}}{\partial \eta} \Big|_{\eta=\delta_c^*(t)} &= 0 \end{aligned} \tag{47}$$

The temperature distribution within the wick is obtained by applying the boundary conditions given by Eq. (46) in the polynomial representation given in Eq. (40). This results in

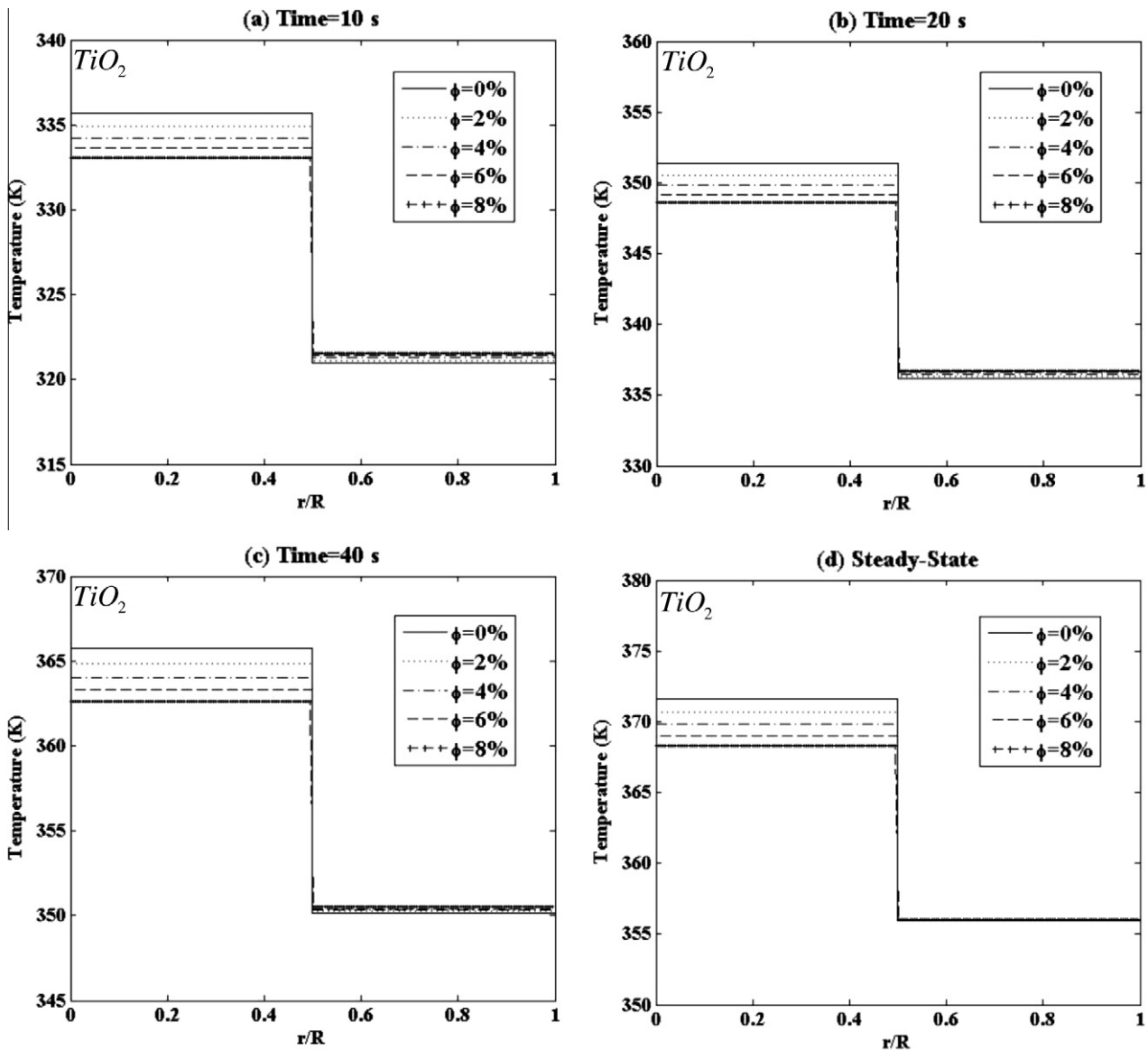


Fig. 11. Disk-shape heat pipe temperature profile for different concentrations of TiO_2 in: (a) 10 s (b) 20 s (c) 40 s and (d) steady state condition.

$$T_l(\eta, t) = T_{l,c}(t) + (T_{lv}(t) - T_{l,c}(t)) \left(1 - \frac{\eta}{h_w}\right)^2 + \frac{q_{l,c}(t)}{\lambda_{eff}} \frac{\eta}{h_w} \left(1 - \frac{\eta}{h_w}\right), \quad 0 \leq \eta \leq h_w, \quad t \geq t_3 \quad (48)$$

Likewise the temperature distribution within the wall for this period can be obtained by applying the boundary conditions given by Eq. (47) to the second order polynomial representation to obtain

$$\frac{T_{wa}(\eta, t) - T_i}{T_{l,c}(t) - T_i} = \left(1 - \frac{\eta - h_w}{\delta_c^*(t) - h_w}\right)^2, \quad h_w \leq \eta \leq \delta_c^*(t), \quad t \geq t_3 \quad (49)$$

There are three unknown variables within the temperature profiles representing the wick and the wall regions as described by Eqs. (48) and (49) respectively. These are $T_{l,c}(t)$, $\delta_c^*(t)$ and $q_{l,c}(t)$. The first one, i.e., $T_{l,c}(t)$ can be found by applying the interface jump condition at the wall–wick interface:

$$T_{l,c}(t) = T_i + \frac{q_{l,c}(t)}{2k_{wa}} (\delta_c^*(t) - h_w) \quad (50)$$

Substituting the temperature distribution given by Eq. (49) in the integrated form of the energy equation (38) with respect to η from h_w to $\delta_c^*(t)$ while using the initial condition $\delta_c^*(t = t_3) = h_w$ yields the second unknown, $\delta_c^*(t)$ as:

$$\delta_c^*(t) = h_w + \sqrt{8\alpha_{wa}(t - t_3)} \quad (51)$$

The time for reaching the thermal layer to the outer wall section can be obtained from Eq. (51) as

$$t_4 = t_3 + \frac{h_w^2}{8\alpha_{wa}} \quad (52)$$

The third unknown, $q_{l,c}(t)$ can be obtained by using the temperature profile within the wick region given by Eq. (48), in the integrated energy Eq. (39) for the wick, with respect to η from 0 to h_w . This results in the following differential equation for the unknown heat flux, $q_{l,c}(t)$ at the interface between the wall and the wick

$$\frac{dq_{l,c}(t)}{dt} = -\frac{16\alpha_{eff}}{h_w^2} \left[\left(1 + \frac{k_{eff}}{k_{wa}h_w} \sqrt{2\alpha_{wa}(t - t_3)}\right) q_{l,c}(t) - \frac{k_{eff}}{h_w} (T_{lv}(t) - T_i) \right] \quad (53)$$

The heat flux at the vapor–liquid interface within this period of time $t_3 \leq t \leq t_4$ can be obtained by using the jump heat flux condition at the wick–vapor interface. This results

$$q_{lv,c}(t) = \frac{2k_{eff}}{h_w} (T_{lv}(t) - T_i) - \left(1 + \frac{k_{eff}}{k_{wa}} \sqrt{\frac{8\alpha_{wa}}{h_w^2}(t - t_3)}\right) q_{l,c}(t) \quad (54)$$

The third stage of the solution corresponds to the physical condition where the thermal layer inside the wall touches the outer surface of the wall and the convection with outside occurs at that interface. During this stage the heat transfer within the wick and

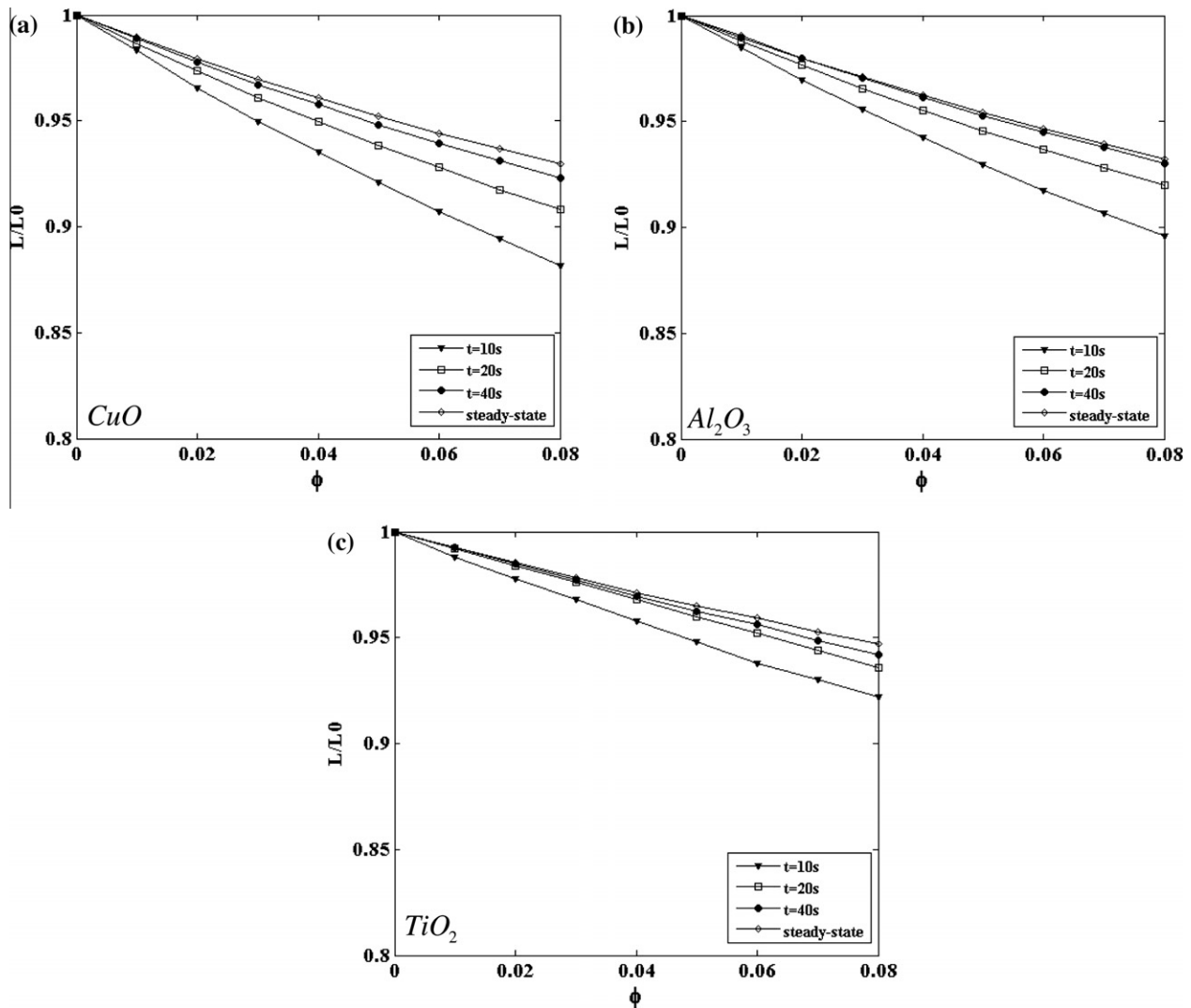


Fig. 12. Concentration effect of nanoparticles on flat-plate heat pipe size for different times and different particles: (a) CuO , (b) Al₂O₃, and (c) TiO₂.

wall regions increase until the heat transfer rate between inside and outside of the wall at the condenser section becomes equal under steady state conditions. The boundary conditions for the wick section are the same as those specified by Eq. (46). However the wall boundary conditions change as follows:

$$\begin{aligned}
 -k_{wa} \frac{\partial T_{wa}}{\partial \eta} \Big|_{\eta=h_w+h_{wa}} &= h_{conv}(T_{wa}(\eta = h_w + h_{wa}, t) - T_{\infty}) \\
 T_{wa}(\eta = h_w, t) &= T_{l,c}(t) \\
 -k_{wa} \frac{\partial T_{wa}}{\partial \eta} \Big|_{\eta=h_w} &= q_{l,c}(t)
 \end{aligned}
 \tag{55}$$

Applying the boundary conditions (46) and (55) to a quadratic temperature distribution as in Eq. (40) results in the temperature distributions in the liquid and wall sections respectively:

$$T_l(\eta, t) = T_{l,c}(t) + (T_{lv}(t) - T_{l,c}(t)) \left(1 - \frac{\eta}{h_w}\right)^2 + \frac{q_{l,c}(t)}{\lambda_{eff}} \frac{\eta}{h_w} \left(1 - \frac{\eta}{h_w}\right),$$

$$0 \leq \eta \leq h_w, \quad t \geq t_4 \tag{56}$$

$$\begin{aligned}
 T_{wa}(\eta, t) &= T_{l,c}(t) - \frac{q_{l,c}(t)}{k_{wa}}(\eta - h_w) \\
 &+ \left(\frac{1 + Bi_{wa}}{2 + Bi_{wa}} \frac{q_{l,c}(t)}{k_{wa}h_{wa}} - \frac{Bi_{wa}}{2 + Bi_{wa}} \frac{T_{l,c}(t) - T_{\infty}}{h_{wa}^2} \right) (\eta - h_w)^2, \\
 h_w \leq \eta \leq h_w + h_{wa}, \quad t \geq t_4
 \end{aligned}
 \tag{57}$$

where $Bi_{wa} = h_{conv}h_{wa}/k_{wa}$.

Substituting the liquid temperature distribution (56) in the integrated form of energy equation (39) with respect to η from 0 to h_w results in a differential equation for $T_{l,c}(t)$

$$\frac{dT_{l,c}(t)}{dt} = -\frac{h_w}{4k_{eff}} \frac{dq_{l,c}(t)}{dt} - \frac{2\alpha_{eff}}{k_{eff}h_w} q_{l,c}(t) + \frac{2\alpha_{eff}}{h_w^2} (T_{lv}(t) - T_{l,c}(t)) \tag{58}$$

Using the wall temperature distribution (57) in the integrated form of the energy Eq. (38), which is obtained by integrating it from $\eta = h_w$ to $h_w + h_{wa}$ yields a second order differential equation which should be solved for the second unknown in the temperature distribution equations, $q_{l,c}(t)$.

$$\begin{aligned}
 \frac{dq_{l,c}(t)}{dt} = & \left\{ -\left(\frac{2Bi_{wa}(1+Bi_{wa})}{t_1} + \frac{Bi_w(3+Bi_{wa})}{t_2-t_1} \right) q_{l,c}(t) \right. \\
 & \left. + \frac{2Bi_{wa}h_{conv}(T_{l,c}(t) - T_{\infty})}{t_1} + \frac{3+Bi_{wa}}{t_2-t_1} h_{conv}(T_{lv}(t) - T_{l,c}(t)) \right\} / \\
 & (Bi_w(Bi_{wa}+3) + Bi_{wa}(Bi_{wa}+4))
 \end{aligned}
 \tag{59}$$

where $Bi_w = h_{conv}h_w/k_{eff}$. The heat flux for the vapor–liquid interface can then be determined by using the interface condition at the wick–vapor interface along with Eqs. (56)–(59)

$$q_{lv,c}(t) = \frac{2k_{eff}}{h_w} (T_{lv}(t) - T_{l,c}(t)) - q_{l,c}(t) \tag{60}$$

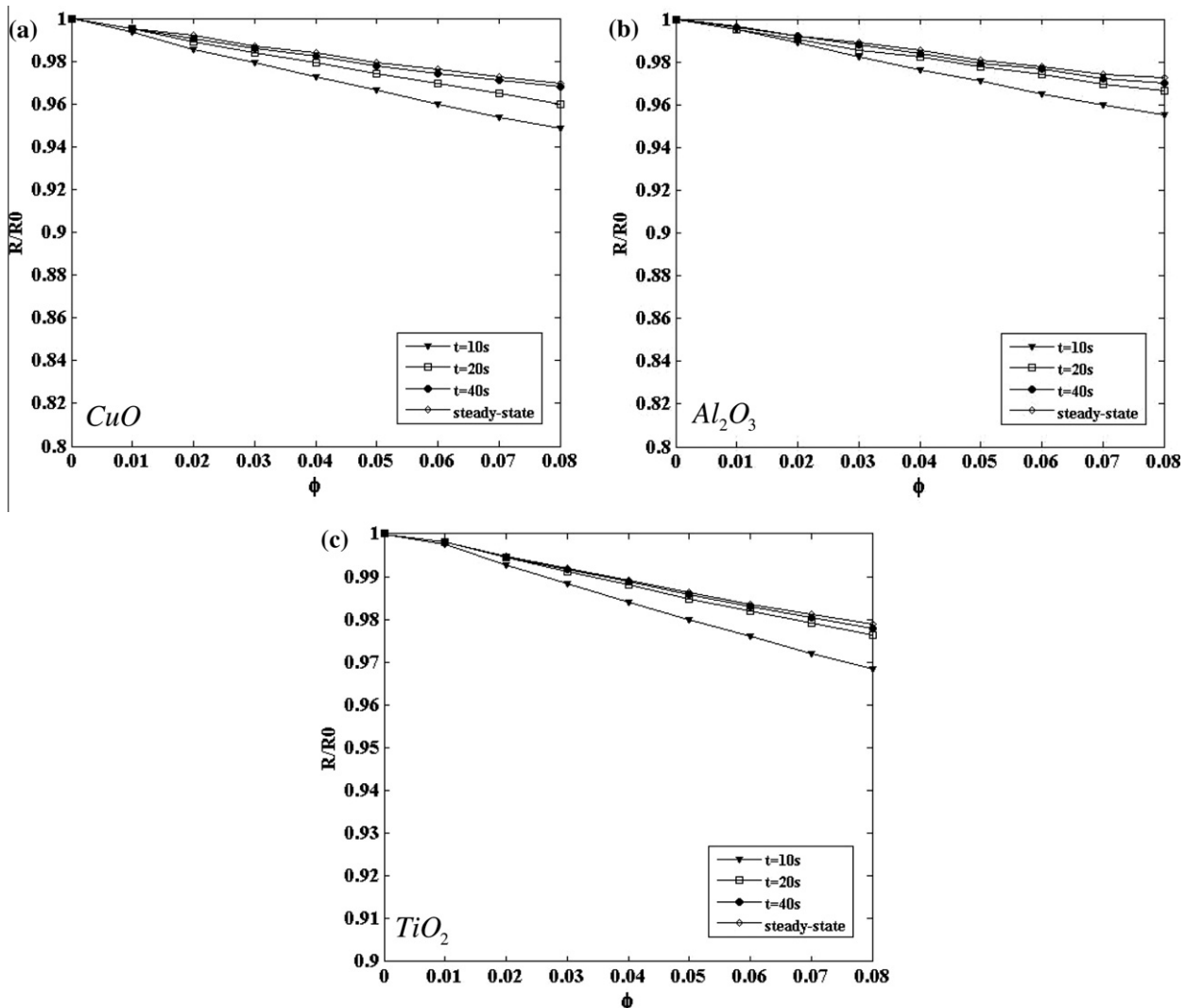


Fig. 13. Concentration effect of nanoparticles on the Disk-shaped heat pipe size for different times and different particles: (a) CuO , (b) Al₂O₃, and (c) TiO₂.

To initiate the solution of the start-up heat pipe problem based on using nanofluids, a marching scheme in time is used. The differential equations for $T_{i,e}(t)$, $q_{i,e}(t)$, $T_{i,c}(t)$ and $q_{i,c}(t)$ are solved. There are two unknowns at each time step namely, the heat flux and temperature at the liquid–vapor interface that require special handling. The initial temperature of the heat pipe forms the basis for initiating the solution for the start up problem. The liquid–vapor temperature (which will be the same as the vapor temperature) is determined based on an overall energy balance specifying the equality between the energy transfer between the evaporator and condenser sections. This is done by determining the heat flux at the evaporator and condenser sections and setting them equal. The new liquid–vapor interface temperature is used for determining the heat fluxes at these two sections. This iterative process continues until the liquid–vapor temperature converges at each time step.

3. Results and discussion

The thermophysical properties of nanofluids were incorporated in the analysis and two asymmetrical flat-shaped heat pipes, namely, flat-plate and disk-shaped were utilized in this work. The outer shell of the heat pipe was assumed to have been made from copper. The dimensions of disk-shaped and flat-plate heat pipes are comparable and are $R = L = 0.25$ m, and the wick and wall thicknesses are chosen as: $h_{wa} = 0.002$ m and $h_w = 0.003$ m. The evaporator heat zone radius for the disk shaped heat pipe and the internal flow channel angle was taken as 0.125 m and 45°,

respectively. The width of channel for the flat-plate heat pipe was taken as 0.06 m. The porosity of the bottom and wall wicks were taken as 0.61 and it was considered to have been made from sintered copper powder. The initial temperature of the heat pipe was taken to be at the room temperature (296 K) and the outer wall fluid heat transfer coefficient was taken as $1200 \text{ W m}^{-2} \text{ K}^{-1}$ at the same room temperature. A heat load of 25 kW was considered to have been uniformly imposed on the outer skin of the heat pipe. The dimensions adopted here are the same as those used in the work of Zhu and Vafai [12]. This enables a more direct comparison of the current results with those presented in Zhu and Vafai [12] which effectively correspond to a zero percent concentration of nanofluids. The results obtained in this work were found to be in excellent agreement with those of Zhu and Vafai [12] as seen in Fig. 4. It should be noted that we can easily obtain the values corresponding to other specification from the presented analytical solution. However, the main features presented and discussed here stay the same for these different values.

Nanofluids used in this research were water based and made from three different primary nanoparticles, namely Al_2O_3 , CuO and TiO_2 . The effects of different concentration levels and different nanoparticles on the temperature distribution, thermal performance, thermal resistance, and size reduction of the flat-shaped heat pipes during the start-up process and leading to the steady state conditions were evaluated. Some of the aspects for thermal resistance and performance of heat pipes in terms of using nanofluids are given in [37,38]. It should be noted that aspects related to latent heat storage could also be incorporated within this analysis to further alter the operational characteristics of the heat pipe [39].

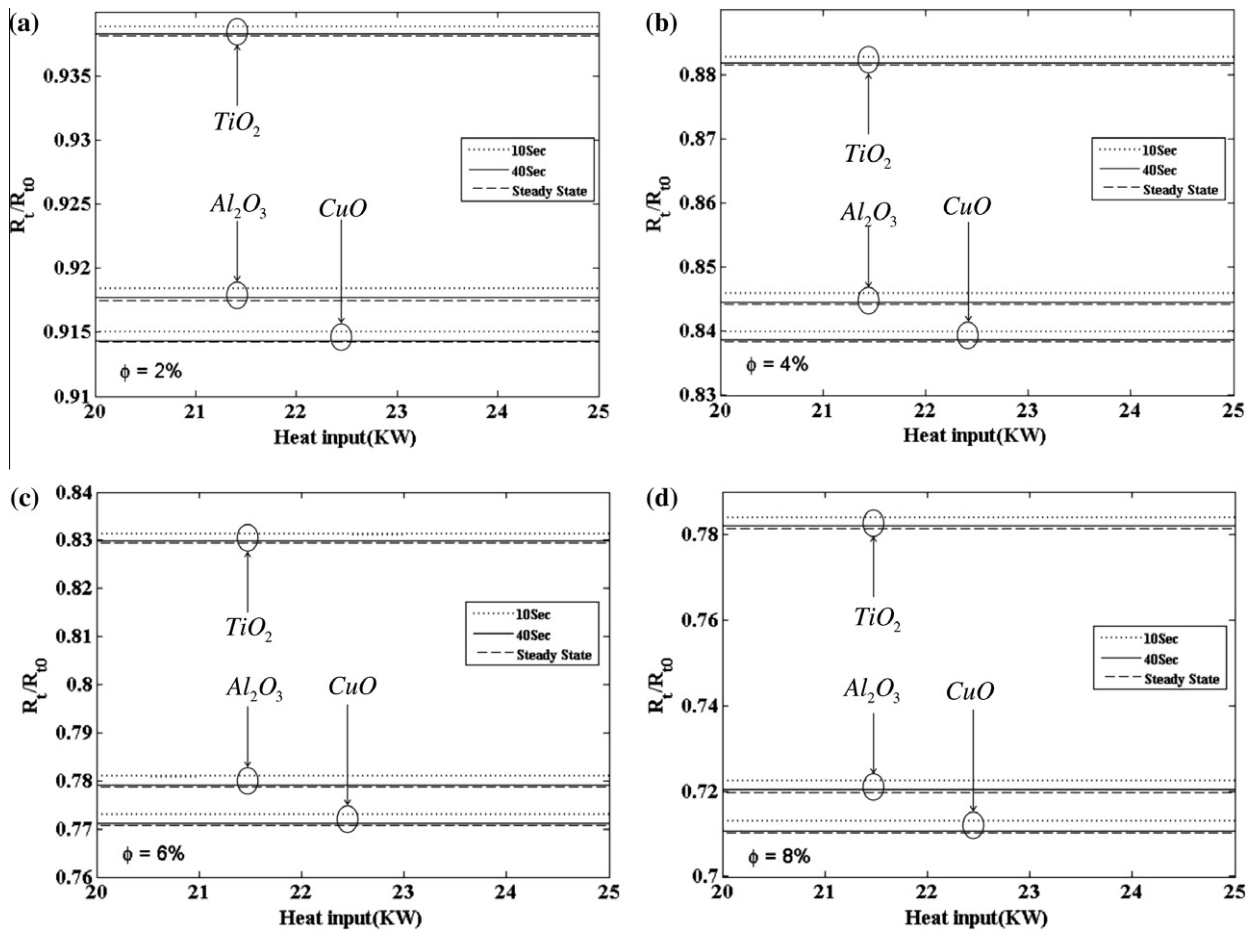


Fig. 14. Concentration level effect in different times on heat pipe thermal resistance: (a) $\phi = 2\%$, (b) $\phi = 4\%$, (c) $\phi = 6\%$, and (d) $\phi = 8\%$.

For example, the time required for the thermal layer to reach the liquid–vapor interface for a regular base fluid was 0.045 s whereas for a two percent concentration of CuO , and TiO_2 nanofluids the time is reduced to 0.041 and 0.042 s, respectively. For an eight percent concentration of CuO and TiO_2 of nanoparticles this time is further reduced to 0.033 and 0.035 s respectively. One of the reasons for these time reductions is the larger thermal diffusivity of copper wall and sintered copper wick in the presence of nanofluids.

Fig. 5 displays the temporal temperature response for different types and concentrations of nanoparticles within the nanofluid for flat-plate and disk-shaped heat pipes. The results clearly show the largest temperature reduction occurring at highest concentration of nanoparticles. The most effective temperature reduction occurs for CuO nanoparticles. As can be seen in Fig. 5 temperature rise for the disk-shaped heat pipe is larger than its counterpart for the flat-plate heat pipe. This is due to the larger condenser area of the flat-plate heat pipe as compared to the disk-shaped heat pipe.

Figs. 6–11 show the wall temperature distributions at different times for three primary nanofluids, for the flat-plate and disk-shaped heat pipes. The three primary nanofluids were based on the use of CuO , Al_2O_3 and TiO_2 nanoparticles. The presented results show the effect of different concentration of nanofluids on the wall temperature. For example, for the flat-plate heat pipe and a CuO based nanofluid at 10 s, a 2% and 8% nanoparticle concentration can result in a 2.08% and 7.08% change in temperature respectively as compared to the case of pure fluid. For the steady state condition this change of temperature becomes 1.54% and 5.22% respectively for the cited cases as can be seen in Fig. 6. These corresponding changes in temperature can be seen in Fig. 7 for the Al_2O_3 based nanofluid. It can be seen from this figure that the corresponding numbers for the Al_2O_3 and TiO_2 based nanofluids after 10 s are 1.85% and 6.25%; and 1.34% and 4.69% while at steady state these changes are 1.46% and 4.96%; and 1.09% and 3.84% respectively.

Similar changes can be observed for the wall temperature distributions for disk-shaped heat pipes shown in Figs. 9–11. It can be seen in Figs. 6–11 that the main temperature reduction occurs in the evaporator section of the flat-shaped heat pipes while the reduction within the condenser section is significantly smaller and less than 1%. This is because of the smaller overall thermal capacity of the evaporator section as compared to the condenser section which in turn is due to the substantially larger condenser area as compared to the evaporator area.

Figs. 12 and 13 show the reduction in the size of flat-plate and disk-shaped heat pipes when using different types of nanofluids as the working fluid. In these graphs, L_0 is the nominal length of water based flat-plate heat pipe and R_0 is the nominal radius for a disk-shaped heat pipe. The results presented in these figures clearly show that if the working fluid in the heat pipe is replaced with a nanofluid, a smaller size heat pipe of the same type could remove the same imposed heat load. As expected, the best size reduction occurs for the CuO based nanofluid as compared to Al_2O_3 and TiO_2 based nanofluids.

One of the important factors in design and operation of a heat pipe is the thermal resistance of the heat pipe and its capability in transferring heat, as for example in the case of electronic cooling. The thermal resistance of a heat pipe can be defined as

$$[q_m/(T_e - T_c)]^{-1}$$

Fig. 14 shows the reduction in the thermal resistance for the flat-shaped heat pipe when using nanofluids. The results are presented for a range of heat load variations from 20 to 25 kW. It can be seen that an increase in nanoparticle concentration results in a reduction in the thermal resistance of the flat-shaped heat pipe, thus resulting in a higher performance. It should be noted that very similar results are also obtained for the case of disk-shaped heat pipe. Finally the

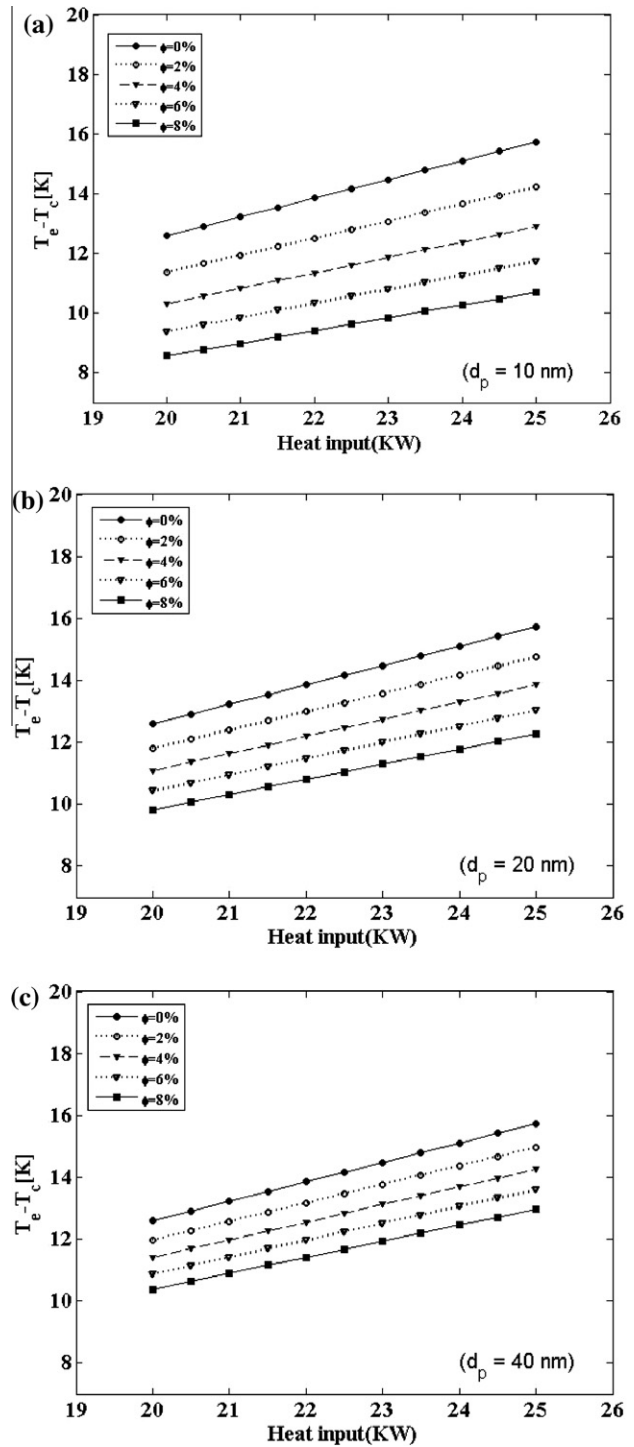


Fig. 15. Effect of the nanoparticle variations on the temperature difference between the evaporator and condenser sections: (a) $d_p = 10$ nm, (b) $d_p = 20$ nm, (c) $d_p = 40$ nm.

effect of variations in the diameter of nanoparticles is shown in Fig. 15. It can be seen that variations in the nanoparticle diameter beyond 20 nm have little effect on the results.

4. Conclusions

Transient behavior, performance, and operational characteristics of flat-shaped heat pipes using nanofluids as the working fluid

are investigated in this work. The presented work incorporates an analytical model to investigate and characterize the transient response of the heat pipe and the wall temperature distribution and temporal response for different types and concentrations of nanofluids. The results demonstrate that a higher percentage of nanoparticles will result in a better performance for the flat-shaped heat pipes. This work clearly demonstrates and quantifies the impact of using different types and concentrations of nanofluids on reducing the size and thermal resistance of the flat-shaped heat pipes under a given imposed load.

References

- [1] M. Shafahi, V. Bianco, K. Vafai, O. Manca, An investigation of the thermal performance of cylindrical heat pipes using nanofluids, *Int. J. Heat Mass Transfer* 53 (1–3) (2010) 376–383.
- [2] M. Shafahi, V. Bianco, K. Vafai, O. Manca, Thermal performance of flat-shaped heat pipes using nanofluids, *Int. J. Heat Mass Transfer* 53 (7–8) (2010) 1438–1445.
- [3] K. Vafai, W. Wang, Analysis of flow and heat transfer characteristics of an asymmetrical flat plate heat pipe, *Int. J. Heat Mass Transfer* 35 (9) (1992) 2087–2099.
- [4] K. Vafai, N. Zhu, W. Wang, Analysis of asymmetric disk-shaped and flat-plate heat pipes, *J. Heat Transfer* 117 (1) (1995) 209–218.
- [5] Y. Wang, K. Vafai, Transient characterization of flat plate heat pipes during startup and shutdown operations, *Int. J. Heat Mass Transfer* 43 (15) (2000) 2641–2655.
- [6] Y. Wang, K. Vafai, An experimental investigation of the thermal performance of an asymmetrical flat plate heat pipe, *Int. J. Heat Mass Transfer* 43 (15) (2000) 2657–2668.
- [7] Y. Wang, K. Vafai, An experimental investigation of the transient characteristics on a flat-plate heat pipe during startup and shutdown operations, *J. Heat Transfer* 122 (3) (2000) 525–535.
- [8] X.F. Yang et al., Heat transfer performance of a horizontal micro-grooved heat pipe using CuO nanofluid, *J. Microeng. Microeng.* 18 (3) (2008) 035038.
- [9] N. Zhu, K. Vafai, The effects of liquid–vapor coupling and non-Darcian transport on asymmetrical disk-shaped heat pipes, *Int. J. Heat Mass Transfer* 39 (10) (1996) 2095–2113.
- [10] N. Zhu, K. Vafai, Numerical and analytical investigation of vapor flow in a disk-shaped heat pipe incorporating secondary flow, *Int. J. Heat Mass Transfer* 40 (12) (1997) 2887–2900.
- [11] N. Zhu, K. Vafai, Vapor and liquid flow in an asymmetrical flat plate heat pipe: a three-dimensional analytical and numerical investigation, *Int. J. Heat Mass Transfer* 41 (1) (1998) 159–174.
- [12] N. Zhu, K. Vafai, Analytical modeling of the startup characteristics of asymmetrical flat-plate and diskshaped heat pipes, *Int. J. Heat Mass Transfer* 41 (17) (1998) 2619–2637.
- [13] N. Zhu, K. Vafai, Analysis of cylindrical heat pipes incorporating the effects of liquid–vapor coupling and non-Darcian transport – a closed form solution, *Int. J. Heat Mass Transfer* 42 (18) (1999) 3405–3418.
- [14] A. Faghri, *Heat Pipe Science and Technology*, Taylor & Francis, 1995.
- [15] S.-W. Kang, W.-C. Wei, S.-H. Tsai, S.-Y. Yang, Experimental investigation of silver nano-fluid on heat pipe thermal performance, *Appl. Thermal Eng.* 26 (17–18) (2006) 2377–2382.
- [16] S.-W. Kang, W.-C. Wei, S.-H. Tsai, C.-C. Huang, Experimental investigation of nanofluids on sintered heat pipe thermal performance, *Appl. Thermal Eng.* 29 (5–6) (2009) 973–979.
- [17] Y.-H. Lin, S.-W. Kang, H.-L. Chen, Effect of silver nano-fluid on pulsating heat pipe thermal performance, *Appl. Therm. Eng.* 28 (11–12) (2008) 1312–1317.
- [18] H.B. Ma, C. Wilson, B. Borgmeyer, K. Park, Q. Yu, S.U.S. Choi, M. Tirumala, Effect of nanofluid on the heat transport capability in an oscillating heat pipe, *Appl. Phys. Lett.* 88 (14) (2006) 143113–143116.
- [19] H.B. Ma, C. Wilson, Q. Yu, K. Park, U.S. Choi, M. Tirumala, An experimental investigation of heat transport capability in a nanofluid oscillating heat pipe, *J. Heat Transfer* 128 (11) (2006) 1213–1216.
- [20] P. Naphon, P. Assadamongkol, T. Borirak, Experimental investigation of titanium nanofluids on the heat pipe thermal efficiency, *Int. Commun. Heat Mass* 35 (10) (2008) 1316–1319.
- [21] P. Naphon, D. Thongkum, P. Assadamongkol, Heat pipe efficiency enhancement with refrigerant–nanoparticles mixtures, *Energy Convers. Manage.* 50 (3) (2009) 772–776.
- [22] J.M. Tournier, M.S. El-Genk, A heat pipe transient analysis model, *Int. J. Heat Mass Transfer* 37 (5) (1994) 753–762.
- [23] C.Y. Tsai, H.T. Chien, P.P. Ding, B. Chan, T.Y. Luh, P.H. Chen, Effect of structural character of gold nanoparticles in nanofluid on heat pipe thermal performance, *Mater. Lett.* 58 (9) (2004) 1461–1465.
- [24] M. Thomson, C. Ruel, M. Donato, Characterization of a flat plate heat pipe for electronic cooling in a space environment, in: *National Heat Transfer Conference Philadelphia, PA HTD*, 1989, pp. 59–65.
- [25] W.S. Chang, G.T. Colwell, Mathematical modeling of the transient operating characteristics of a low-temperature heat pipe, *Numer. Heat Transfer* 8 (2) (1985) 169–186.
- [26] S.-Q. Zhou, R. Ni, Measurement of the specific heat capacity of water-based Al₂O₃ nanofluid, *Appl. Phys. Lett.* 92 (9) (2008) 093123.
- [27] S.U.S. Choi, J.A. Eastman, Enhancing thermal conductivity of fluids with nanoparticles.
- [28] B.C. Pak, Y.I. Cho, Hydrodynamic and heat transfer study of dispersed fluids with submicron metallic oxide particles, *Exp. Heat Transfer* 11 (2) (1998) 151–170.
- [29] H.C. Brinkman, The viscosity of concentrated suspensions and solutions, *J. Chem. Phys.* 20 (4) (1952) 571.
- [30] K.H. Do, S.P. Jang, Effect of nanofluids on the thermal performance of a flat micro heat pipe with a rectangular grooved wick, *Int. J. Heat Mass Transfer* 53 (9–10) (2010) 2183–2192.
- [31] Z.-h. Liu, J.-g. Xiong, R. Bao, Boiling heat transfer characteristics of nanofluids in a flat heat pipe evaporator with micro-grooved heating surface, *Int. J. Multiphase Flow* 33 (12) (2007) 1284–1295.
- [32] R.R. Riehl, Analysis of loop heat pipe behavior using nanofluid, in: *Heat Powered Cycles International Conference (HPC)*, New Castle, UK, Paper 06102, 2006.
- [33] J.-M. Tournier, M.S. El-Genk, A.J. Juhasz, Heat-pipe transient model for space applications, *AIP Conf. Proc.* 217 (2) (1991) 857–868.
- [34] P.D. Dunn, D.A. Reay, *Heat Pipes*, Pergamon Press, 1976.
- [35] W. Yu, S.U.S. Choi, The role of interfacial layers in the enhanced thermal conductivity of nanofluids: a renovated Maxwell model, *J. Nanoparticle Res.* 5 (1) (2003) 167–171.
- [36] K. Khanafer, K. Vafai, A critical synthesis of thermophysical characteristics of nanofluids, *Int. J. Heat Mass Transfer* 54 (19–20) (2011) 4410–4428.
- [37] K.H. Do, H.J. Ha, S.P. Jang, Thermal resistance of screen mesh wick heat pipes using the water-based Al₂O₃ nanofluids, *Int. J. Heat Mass Transfer* 53 (25–26) (2010) 5888–5894.
- [38] J. Qu, H.Y. Wu, P. Cheng, Thermal performance of an oscillating heat pipe with Al₂O₃–water nanofluids, *Int. Commun. Heat Mass Transfer* 37 (2010) 111–115.
- [39] K. Vafai, M. Sozen, An investigation of a latent heat storage porous bed and condensing flow through it, *ASME J. Heat Transfer* 112 (1990) 1014–1022.